Remodeling and activation mechanisms of outer arm dynein revealed by cryo-EM

Shintaroh Kubo[1,2,Ψ], Shun Kai Yang[1,Ψ], Corbin Black[1], Daniel Dai[1], Melissa Valente[1], Jacek Gaertig[3], Muneyoshi Ichikawa[4,5,*], Khanh Huy Bui[1,6,*]

Cilia are thin microtubule-based protrusions of eukaryotic cells, beating at high frequency to propel the cell in sperms or clear mucus in the respiratory tract. The ciliary beating is driven by the outer arm dynein arms (ODAs) which anchor on the doublet microtubules. Here, we report the ODA complex structure from the native doublet microtubules by cryo-electron microscopy. Our structure reveals how the ODA complex is attached to the doublet microtubule via the docking complex in its native state. Combined with molecular dynamics simulations, we present a model of how the attachment of the ODA complex to the doublet microtubule induces rearrangements and activation mechanisms within the ODA complex.

Author affiliations

1. Department of Anatomy and Cell Biology, McGill University, Montréal, Québec H3A 0C7, Canada
2. JSPS Overseas Research Fellow
3. Department of Cellular Biology, University of Georgia, Athens, GA 30602, USA
4. Department of Systems Biology, Graduate School of Biological Sciences, Nara Institute of Science and Technology, Ikoma, Nara 630-0192, Japan
5. PRESTO, Japan Science and Technology, Kawaguchi, Saitama, 332-0012, Japan
6. Centre de Recherche en Biologie Structurale, McGill University, Montréal, Québec H3A 0C7, Canada

*Corresponding authors:
Muneyoshi Ichikawa, e-mail: michikawa@bs.naist.jp
Khanh Huy Bui, e-mail: huy.bui@mcgill.ca

In eukaryotes, cilia are responsible for cell motility. These microscopic hair-like organelles bend several tens of times per second to generate fluid flows. Cilia in trachea generate the flow of mucus and protect our body from infectious agents such as viruses. Motile cilia have a canonical axonemal 9+2 structure where the central pair microtubules are surrounded by nine doublet microtubules (DMTs) (Fig. 1A). The main propulsive force generators are the outer dynein arms (ODA) (*1*), thus, improper assembly of the ODA complex causes ciliopathies in humans (reviewed in (*2*)).

In *Tetrahymena*, the ODA complex is composed of three heavy chains (HCs) (Dyh3, 4 and 5), two intermediate chains (IC2 and IC3) and numerous light chains (LCs). Each HC has a head and tail domain. The three heads are coupled together by their tail domains. Within each head domain, there is an AAA+ ring where ATP is hydrolyzed to produce force. The ODA complex stably attach stably attaches to the A-tubule of the DMT and exerts force on the B-tubule of the neighboring DMT (Fig. 1A). The docking of the ODA complex to the A-tubule is mediated by the tail domain. The interaction with the neighboring B-tubule is mediated by the microtubule binding domain (MTBD) at the tip of the stalk which extends from the AAA+ ring. ICs and LCs have various regulatory roles (reviewed in (*1*)). The ODA complex attached to the DMT has been studied by cryo-electron tomography (cryo-ET) of the intact axoneme (*3-5*). However, the resolution of the ODA on the doublet remains only in the range of 20-40 Å, which does not resolve any subunit organization. Here, using single-particle cryo-electron microscopy (cryo-EM), we obtained the native ODA complex structure with a 7.8 Å resolution using K40R and MEC17-KO *Tetrahymena* mutants (Fig. 1 and S1, see also Materials and Methods). The resolutions of the tail region, Dyh3 and Dyh4 head parts were improved to 5.5 Å, 5.8 Å and 7 Å by focused refinement (Fig.1D and S2).

We built in all the components of the ODA complex except for Dyh5's head due to the flexibility of this region (Fig. 1, see Materials and Methods). Even without Dyh5, our model still represents the conserved components of the ODA complex since Dyh5 is not conserved in vertebrates (*6*). Part of the docking complex (DC) on the DMT was also visualized in our structure (Fig. 2 and Fig. S3A). We identified *Tetrahymena* proteins Q22T00, Q233H6 and I7M2C6 as DC1/2/3 following the names of the counterparts of *Chlamydomonas reinhardtii* (Fig.S3B and C, see Materials and Methods for details). Along the DMT, DC1/2 forms a 24-nm coiled coil repeating unit, the same periodicity as the repeating unit of the ODA complex. DC3 associates with the DC1/2 coiled coil region on the DMT consistent with a previous study (*7*). A part of the Dyh3-HC's α-helix bundle-3

interacts with DC3 (Fig. 2C). DC1/2 appears to connect to coiled-coil density associated with the neighboring ODA tail domain (dashed lines in Fig. 2A, and Fig. S3H). The tethering of the ODA to the DMT io mediated by Dyh3 alone and ICs/LCs are not involved.

The two-site attachment of the ODA by the DC is likely to be crucial for the stable anchoring of the ODA complex to the DMT, and therefore, force generation by the ODA complex within the cilia. The ODA complex is bottomed up by DC "heals" so that it can associate with the neighboring DMT properly. DC3 in *Tetrahymena* and *Chlamydomonas* contains several EF-hand motifs. It is possible that the interaction of DC3 to the ODA complex can change based on the intracellular calcium ion concentration, leading to the regulation of ODA activity (*8, 9*).

It has been recently shown that the ODA complex, before its assembly on the DMT, is in an inactive form bound to the regulatory protein Shulin (*10*). To understand how the ODA rearranges into an active form on the DMT, the two structures were compared (Fig. 2E and F, and Fig. S4). The overall appearance of the active ODA complex was more compact compared with the inactive ODA complex since its heads have their linker domains in a post-powerstroke conformation (Fig. S5, Supplementary text). The region undergoing the least conformation change between the two structures is the tail of the Dyh4 HC up to the bundle-4 region where the DIC3's WD40 domain resides (Fig. 2F). During activation, Dyh3 HC, DIC2 and LC tower rotate together by ~90° along the long axis of the HC, relative to the Dyh4's base region. With this configuration change, the Dyh3 and Dyh4 HCs no longer cross to each other and are freed. In the active conformation, DIC2's WD40 domain interacts with the Dyh4 HC, and the WD40 domain of DIC3 is docked onto the Dyh3 HC (Fig. 2F). Within the HCs, there were also conformational changes (Fig. S4B). The tail rearrangements align the head domains to parallel configuration on the DMT.

We sought how the regulatory protein Shulin detaches from the ODA complex. The base region of the Dyh4 tail does not change significantly upon docking to the DMT (Fig. 3A). In contrast, the tail region of Dyh3 is remodeled and located closer to the DMT (Fig. 3A-C). This remodeled region coincides with the part which interacts with DC3 and both coiled-coil regions of the extended DC1/2 (Fig. coiled-coil regions of the extended DC1/2 (Fig. 3C). Therefore, we hypothesized that the remodeling of the tail causes the detachment of Shulin. To test this idea, we performed a molecular dynamics (MD) simulation mimicking the interaction and remodeling of Dyh3 by applying an external force to Dyh3 of the Shulin-ODA complex (Fig. 3D, see Materials and methods for the details). In nine out of ten MD trajectories, Shulin detached within 1,000 frames

(Fig. 3E). Without external force applied, only two out of ten trajectories showed detachment within 5,000 frames, five times longer than with external force (Fig. 3F). Therefore, the remodeling of Dyh3 induced by interaction with the DC is likely to be important for the Shulin detachment.

Based on our results, we present a model of how the ODA attachment induces remodeling and activation of the ODA complex (Fig. 3G). First, the Shulin-ODA complex docks onto the DMT using DC3 as a marker. Next, the Dyh3 tail region starts to remodel. The extended region of DC1/2 catches the remodeled Dyh3 tail domain. Due to the remodeling in the Dyh3 tail region, the binding of Shulin becomes destabilized. After Shulin detaches, the remodeling is propagated toward the heads, and the head domains are released into a parallel configuration. The interaction of the head domain with the neighboring ODA complex (Supplementary text) would enhance this process.

The remodeling of the tail involves an interaction with the extended coiled-coil part of DC1/2. This is the reminiscence of the cytoplasmic dynein-1's case. The inactive form of cytoplasmic dynein-1 (*11*) is released by the interactions with adaptor proteins, such as BICD2, BICDR1 and HOOK3, which are also coiled coil (*12, 13*). Thus, similar mechanisms are exploited for cytoplasmic dynein-1 and the ODA for the activation. In conclusion, we showed the ODA complex structure on the DMT and obtained insights into how the ODA is activated inside the cilia. Our findings would be the important foundation to understand the assembly of ciliary structure.

Acknowledgements

We thank Drs. Kaustuv Basu, Kelly Sears, Mike Strauss, Ferdos Abid Ali and Andrew P. Carter for helping with data collection, processing and modelling. This work was supported by JST, PRESTO, JSPS KAKENHI Grant Numbers JP19K23726 and JP20K15733, and the Foundation for Nara Institute of Science and Technology (R2290001) to MI. SK is supported by JSPS Overseas Research Fellowships. KHB is supported by the grants from Canadian Institutes of Health Research (PJT-156354), Natural Sciences and Engineering Research Council of Canada (RGPIN-2016-04954) and Canadian Institute for Advanced Research (Arzieli Global Scholar Program).

Conflicts of Interest

The authors declare no conflicts of interest.

Data Availability

Cryo-EM maps have been deposited in EM data bank (EMDB) with accession numbers of EMD-XXXX (the head domain of the ODA complex on the doublet), EMD-XXXX (the tail domain of the ODA complex on the doublet), EMD-XXXX (DC1/2/3 part with part of doublet). The model of the ODA on the doublet is available in Protein Data Bank (PDB) with an accession number of PDB: XXXX.

References And Notes

1. S. M. King, Integrated control of axonemal dynein AAA(+) motors. *J Struct Biol* **179**, 222-228 (2012).
2. J. F. Reiter, M. R. Leroux, Genes and molecular pathways underpinning ciliopathies. *Nat Rev Mol Cell Biol* **18**, 533-547 (2017).
3. T. Oda, T. Abe, H. Yanagisawa, M. Kikkawa, Structure and function of outer dynein arm intermediate and light chain complex. *Mol Biol Cell* **27**, 1051-1059 (2016).
4. K. H. Bui, H. Sakakibara, T. Movassagh, K. Oiwa, T. Ishikawa, Molecular architecture of inner dynein arms in situ in Chlamydomonas reinhardtii flagella. *J Cell Biol* **183**, 923-932 (2008).
5. J. Lin, K. Okada, M. Raytchev, M. C. Smith, D. Nicastro, Structural mechanism of the dynein power stroke. *Nat Cell Biol* **16**, 479-485 (2014).
6. K. Inaba, Calcium sensors of ciliary outer arm dynein: functions and phylogenetic considerations for eukaryotic evolution. *Cilia* **4**, 6 (2015).
7. M. Ma *et al.*, Structure of the Decorated Ciliary Doublet Microtubule. *Cell* **179**, 909-922 e912 (2019).
8. M. Bessen, R. B. Fay, G. B. Witman, Calcium control of waveform in isolated flagellar axonemes of Chlamydomonas. *J Cell Biol* **86**, 446-455 (1980).
9. Y. Satouh *et al.*, Molecular characterization of radial spoke subcomplex containing radial spoke protein 3 and heat shock protein 40 in sperm flagella of the ascidian Ciona intestinalis. *Mol Biol Cell* **16**, 626-636 (2005).
10. G. R. Mali *et al.*, Shulin packages axonemal outer dynein arms for ciliary targeting. *bioRxiv*, (2020).
11. T. Torisawa *et al.*, Autoinhibition and cooperative activation mechanisms of cytoplasmic dynein. *Nat Cell Biol* **16**, 1118-1124 (2014).
12. K. Zhang *et al.*, Cryo-EM Reveals How Human Cytoplasmic Dynein Is Auto-inhibited and Activated. *Cell* **169**, 1303-1314 e1318 (2017).
13. L. Urnavicius *et al.*, Cryo-EM shows how dynactin recruits two dyneins for faster movement. *Nature* **554**, 202-206 (2018).
14. M. A. Gorovsky, M. C. Yao, J. B. Keevert, G. L. Pleger, Isolation of micro- and macronuclei of Tetrahymena pyriformis. *Methods Cell Biol* **9**, 311-327 (1975).

15. D. N. Mastronarde, Automated electron microscope tomography using robust prediction of specimen movements. *J Struct Biol* **152**, 36-51 (2005).
16. S. Q. Zheng *et al.*, MotionCor2: anisotropic correction of beam-induced motion for improved cryo-electron microscopy. *Nat Methods* **14**, 331-332 (2017).
17. J. Zivanov *et al.*, New tools for automated high-resolution cryo-EM structure determination in RELION-3. *Elife* **7**, (2018).
18. K. Zhang, Gctf: Real-time CTF determination and correction. *J Struct Biol* **193**, 1-12 (2016).
19. G. Tang *et al.*, EMAN2: an extensible image processing suite for electron microscopy. *J Struct Biol* **157**, 38-46 (2007).
20. E. H. Egelman, The iterative helical real space reconstruction method: surmounting the problems posed by real polymers. *J Struct Biol* **157**, 83-94 (2007).
21. J. Frank *et al.*, SPIDER and WEB: processing and visualization of images in 3D electron microscopy and related fields. *J Struct Biol* **116**, 190-199 (1996).
22. N. Grigorieff, FREALIGN: high-resolution refinement of single particle structures. *J Struct Biol* **157**, 117-125 (2007).
23. V. Abrishami *et al.*, Localized reconstruction in Scipion expedites the analysis of symmetry mismatches in cryo-EM data. *Prog Biophys Mol Biol*, (2020).
24. J. M. de la Rosa-Trevin *et al.*, Scipion: A software framework toward integration, reproducibility and validation in 3D electron microscopy. *J Struct Biol* **195**, 93-99 (2016).
25. A. Punjani, J. L. Rubinstein, D. J. Fleet, M. A. Brubaker, cryoSPARC: algorithms for rapid unsupervised cryo-EM structure determination. *Nat Methods* **14**, 290-296 (2017).
26. P. Emsley, B. Lohkamp, W. G. Scott, K. Cowtan, Features and development of Coot. *Acta Crystallogr D Biol Crystallogr* **66**, 486-501 (2010).
27. P. V. Afonine *et al.*, Real-space refinement in PHENIX for cryo-EM and crystallography. *Acta Crystallogr D Struct Biol* **74**, 531-544 (2018).
28. B. Webb, A. Sali, Protein structure modeling with MODELLER. *Methods Mol Biol* **1137**, 1-15 (2014).
29. W. Zhang *et al.*, Whole-exome sequencing identifies a novel CCDC151 mutation, c.325G>T (p.E109X), in a patient with primary ciliary dyskinesia and situs inversus. *J Hum Genet* **64**, 249-252 (2019).
30. R. Hjeij *et al.*, CCDC151 mutations cause primary ciliary dyskinesia by disruption of the outer dynein arm docking complex formation. *Am J Hum Genet* **95**, 257-274 (2014).
31. A. B. Dean, D. R. Mitchell, Chlamydomonas ODA10 is a conserved axonemal protein that plays a unique role in outer dynein arm assembly. *Mol Biol Cell* **24**, 3689-3696 (2013).
32. G. J. Pazour, N. Agrin, J. Leszyk, G. B. Witman, Proteomic analysis of a eukaryotic cilium. *J Cell Biol* **170**, 103-113 (2005).
33. D. Dai, M. Ichikawa, K. Peri, R. Rebinsky, K. H. Bui, Identification and mapping of central pair proteins by proteomic analysis. *Biophysics and Physicobiology*, (2020).
34. A. Lupas, M. Van Dyke, J. Stock, Predicting coiled coils from protein sequences. *Science* **252**, 1162-1164 (1991).
35. T. D. Goddard *et al.*, UCSF ChimeraX: Meeting modern challenges in visualization and analysis. *Protein Sci* **27**, 14-25 (2018).
36. W. Li, W. Wang, S. Takada, Energy landscape views for interplays among folding, binding, and allostery of calmodulin domains. *Proc Natl Acad Sci U S A* **111**, 10550-10555 (2014).
37. W. Li, T. Terakawa, W. Wang, S. Takada, Energy landscape and multiroute folding of topologically complex proteins adenylate kinase and 2ouf-knot. *Proc Natl Acad Sci U S A* **109**, 17789-17794 (2012).

38. S. Kubo, W. Li, S. Takada, Allosteric conformational change cascade in cytoplasmic dynein revealed by structure-based molecular simulations. *PLoS Comput Biol* **13**, e1005748 (2017).
39. H. Kenzaki *et al.*, CafeMol: A Coarse-Grained Biomolecular Simulator for Simulating Proteins at Work. *J Chem Theory Comput* **7**, 1979-1989 (2011).
40. K. Toropova *et al.*, Lis1 regulates dynein by sterically blocking its mechanochemical cycle. *Elife* **3**, (2014).
41. M. Ichikawa *et al.*, Axonemal dynein light chain-1 locates at the microtubule-binding domain of the gamma heavy chain. *Mol Biol Cell* **26**, 4236-4247 (2015).
42. A. Toda, Y. Nishikawa, H. Tanaka, T. Yagi, G. Kurisu, The complex of outer-arm dynein light chain-1 and the microtubule-binding domain of the gamma heavy chain shows how axonemal dynein tunes ciliary beating. *J Biol Chem* **295**, 3982-3989 (2020).
43. K. Wakabayashi, S. M. King, Modulation of Chlamydomonas reinhardtii flagellar motility by redox poise. *J Cell Biol* **173**, 743-754 (2006).
44. A. A. Z. Khalifa *et al.*, The inner junction complex of the cilia is an interaction hub that involves tubulin post-translational modifications. *Elife* **9**, (2020).
45. M. Ichikawa *et al.*, Tubulin lattice in cilia is in a stressed form regulated by microtubule inner proteins. *Proceedings of the National Academy of Sciences*, (2019).
46. M. Ichikawa *et al.*, Subnanometre-resolution structure of the doublet microtubule reveals new classes of microtubule-associated proteins. *Nat Commun* **8**, 15035 (2017).
47. D. Stoddard *et al.*, Tetrahymena RIB72A and RIB72B are microtubule inner proteins in the ciliary doublet microtubules. *Mol Biol Cell* **29**, 2566-2577 (2018).

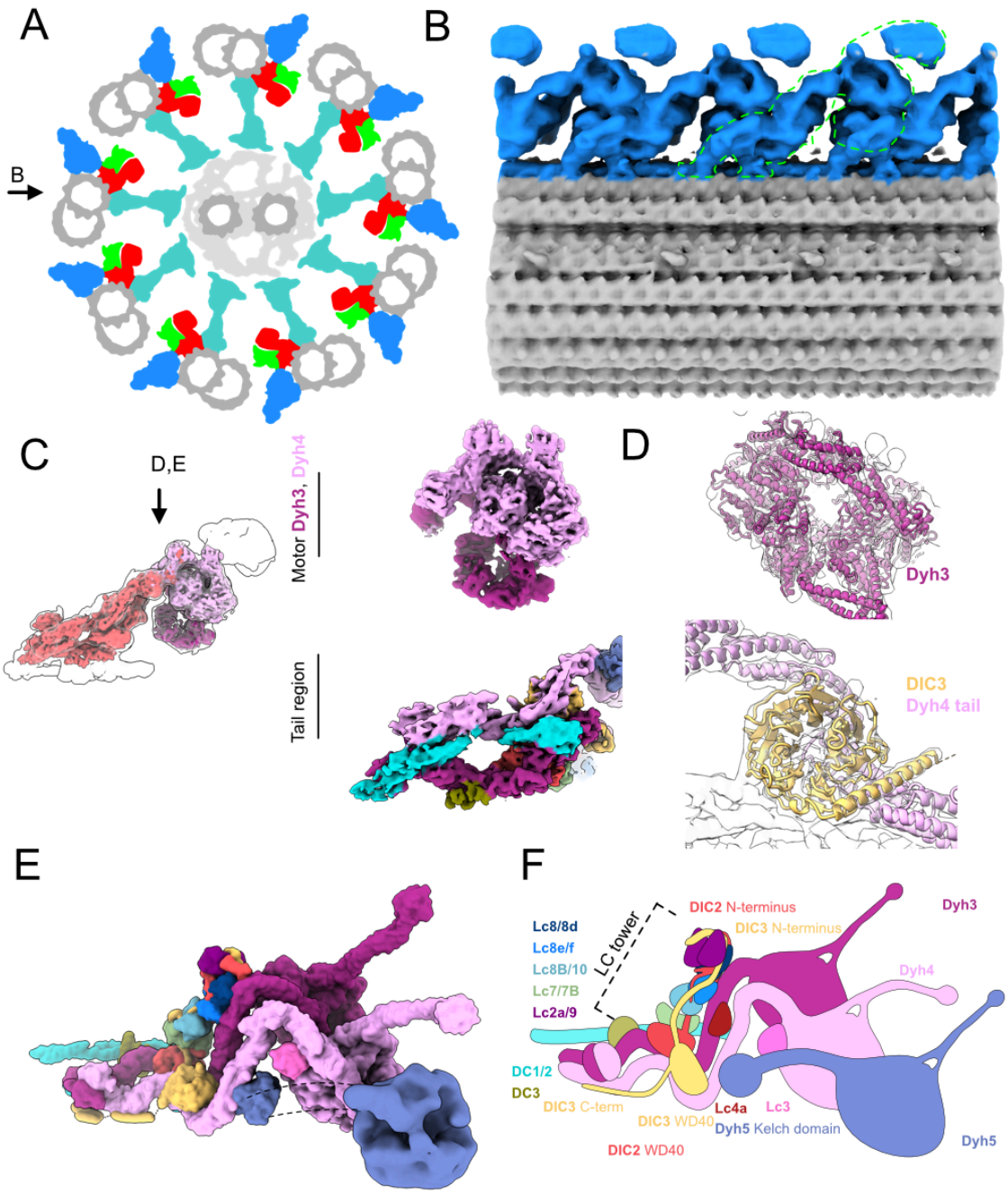

Fig.1 Cryo-EM structure of the ODA complex on the DMT

(A) Schematic diagram of axoneme structure of cilia viewed from the base of the cilia. DMT: gray; ODA: blue; inner dynein arm: red; dynein regulatory complex: green; radial spokes: cyan. Black arrow indicates the view in B. (B) The 24-nm structure of the DMT filtered to 18 Å showing the row of the ODA complexes. The green outline indicates the single ODA complex. (C) A schematic cartoon of the DMT and the ODA complex. Arrow indicates the view in D. (D) The focused refined maps of the tail and the heads of the ODA are shown within the map of the entire ODA complex (left). The focused refined maps of Dyh3 and Dyh4 heads and the tail (right). (E) Fitting of models

into maps (Dyh3, top; DIC3 and Dyh4 tail, bottom). (F, G). The surface render of the model (F) and the schematic cartoon (G) of the ODA with the docking complex. The Dyh5 head is only shown as the 18-Å resolution surface render and the Dyh5 tail is drawn as dotted lines. All the components (ICs, LCs and DCs) are colored and indicated and will be used consistently in all the figures.

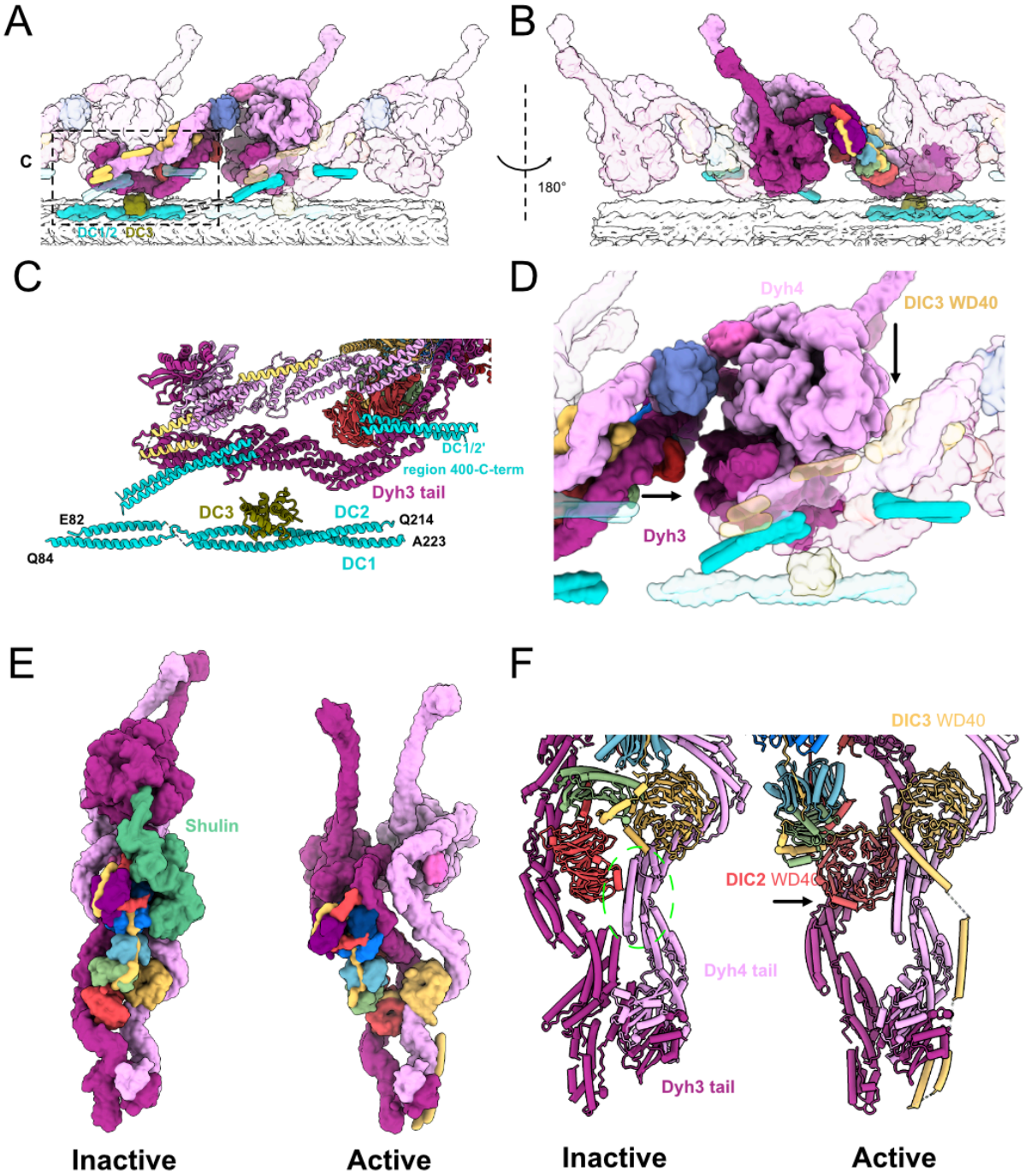

Fig. 2 Interactions between the ODA complex and the DC, and the remodeling of the ODA complex.

(A, B) The stacking of the ODA complexes in the axoneme viewed from inside (A) and outside (B) the cilia. The middle ODA complex is shown in color. The proximal and distal ODA complexes are rendered transparent. (C) Model of the DC and the tail of the ODA. (D) The interaction of the ODA head with the tail of the proximal ODA complex unit. Dyh3 head interacts with the

dimerization domain NDD of the proximal Dyh4. The Dyh4 head interacts with the DIC3 WD40 of the proximal ODA complex. (E) The surface rendering of the inactive ODA model (with Shulin bound) and the active ODA model. Dyh5 is not shown. (F) Remodeling of Dyh3 and Dyh4 tails and associated ICs. The green circle indicates the region of alignment (Dyh4 residues 414-513, helix bundle 3). Dyh4 tail does not exhibit large conformational change while Dyh3 tail rotates almost 90°, evident by the rotation of DIC2 WD40 domain.

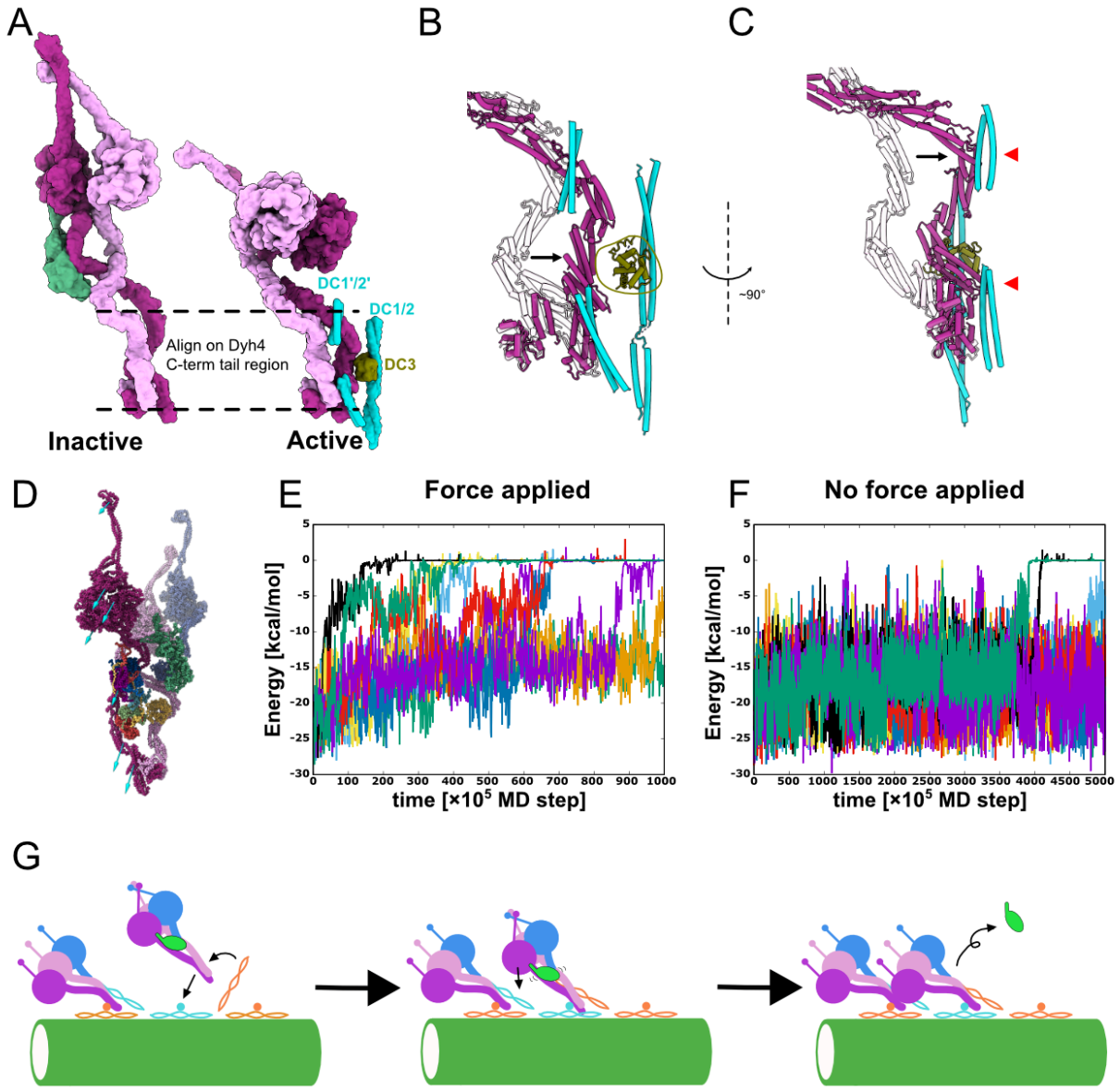

Fig. 3 Remodeling of the tail domain and the Shulin detachment.
(A) Model of the inactive and active ODA Dyh3 and Dyh3 binding to Shulin and docking complex, respectively. The two structures are aligned based on the Dyh4 helix bundle 3. (B, C) Detailed comparison of the Dyh3 before and after the remodeling. With the two structures aligned as in A, Dyh3 tail in the active conformation indicates significant shift towards the DC3 (B). Similarly, the Dyh3 tail in the active conformation showed a significant shift toward the DC1/2 region ~320-400 aa. Red arrowheads indicate the interaction sites of Dyh3 with the DC1/2. (D) Coarse grain molecular dynamics of the inactive Shulin-ODA complex. External force was applied in the direction of the arrow to simulate the remodeling of Dyh3 upon binding to the DMT. (E, F) Energy trajectories between Shulin and the ODA complex with (E) and without (F) external force applied to Dyh3. 8 out of 10 setups showed detachment of Shulin (energy = 0) with external force in 1,000 x 10^5 MD steps (E). In contrast, only 2 out of 10 trajectories showed Shulin detachment without applied force even with 5,000 x 10^5 MD steps (F). These results suggest that Dyh3's tail

remodeling facilitates the Shulin detachment. (G) The Shulin-ODA complex docks on the DMT through interaction between the tail region of Dyh3 and the DC3. Then, the extended region of the DC1/2 catches the ODA complex at the tail domain and "pushes" the Dyh3 facilitating the remodeling of the tail. Head domain of Dyh3 also interacts with the neighboring ODA complex. Therefore, the Dyh3 is "pulled" toward the DMT and binding of the Shulin destabilizes. Finally, Shulin detaches from the ODA complex and the head domains are remodeled and aligned parallel to each other. Head domains are also in post-powerstroke conformations and ready to exert force.

Supplementary Materials & Methods

Growth of *Tetrahymena* cells for isolation

1 mL of the saturated *Tetrahymena* cells in SPP media (*14*) was transferred into 50 mL liquid SPP and grown overnight with shaking at 150 rpm at 30℃ in the shaker incubator (Thermo Fisher Scientific, MAXQ8000). The overnight 50 mL culture was added to 900 mL of SPP and grown for approximately two days with shaking at 150 rpm at 30℃ (MAXQ8000) until the cell density reached an OD at 600 nm of 0.7.

Cilia isolation by dibucaine treatment

The *Tetrahymena* culture was centrifuged at 700xg for 10 min at 22°C with slow deceleration (Avanti, Rotor JLA-8.1000). The cell pellet was resuspended with 10 mL of SPP and the volume was adjusted to 24 mL. The cell suspension was transferred to a 250 mL Erlenmeyer flask on ice. 1 mL dibucaine in SPP at 25 mg/mL was added to the flask to make a final concentration of 1 mg/mL, and the cell suspension was gently swirled over ice for exactly 60 seconds. 75 mL of ice-cold liquid SPP media was immediately added, and the 100 mL cilia suspension was then split into two 50 mL conical tubes. The cell suspension was centrifuged at 2,000xg for 10 min at 4°C with slow deceleration (Sorvall ST 16R, Rotor 75003181). The cilia-containing supernatant was transferred to 4 centrifuge tubes for the Beckman Coulter JA 25.50 rotor, approximately 20 mL per tube. The tubes containing the cilia-containing supernatant were centrifuged at 17,000g for 40 min at 4°C with slow deceleration (Avanti, Rotor JA25.50). The supernatants were discarded, and the pellets were carefully washed with theice-cold Cilia Wash Buffer (50 mM HEPES at pH 7.4, 3 mM MgSO4, 0.1 mM EGTA, 1 mM DTT, 250 mM sucrose), before resuspension in 250 µL of the ice cold Cilia Wash Buffer. The cilia were pelleted by centrifugation with 16,000xg for 10 min at 4°C in a microfuge, flash-frozen with liquid nitrogen and stored in the -80°C.

Purification of the intact DMT

The thawed cilia pellet was resuspended in 250 µL ice-cold Cilia Final Buffer (50 mM HEPES at pH 7.4, 3 mM MgSO4, 0.1 mM EGTA, 1 mM DTT, 0.5% Trehalose, 1 mM PMSF). The

concentration of total protein was measured using the Bradford Assay. The resuspended cilia sample was centrifuged at 16,000g for 10 min at 4°C in a microfuge (Eppendorf, Centrifuge 5415D). The supernatant was discarded, and the pellet was resuspended once more with 250 µl Cilia Final Buffer. NP-40 alternative (Millipore Sigma, 492016) was added to the final concentration of 15% and the total solution was resuspended. The samples were incubated on ice for 30 min before the demembraned cilia were centrifuged at 16,000xg for 10 min at 4°C in a microfuge (Eppendorf, Centrifuge 5415D). The supernatant was discarded, and the axoneme-containing pellet was resuspended to 245 µL of Cilia Final Buffer. Final concentration of 1 mM ADP was added to the axonemes and incubated at room temperature for 10 minutes. Then, final concentration of 0.1 mM ATP was added to the solution and incubated at the room temperature for 10 minutes (Fig. S1A).

Cryo-EM sample preparation

Wild-type, K40R and MEC17-KO doublet concentrations were adjusted to 3 mg/mL. Quantifoil R2/2 (Electron Microscopy Sciences, #Q2100CR2) were treated with chloroform overnight and then glow discharged (30 seconds at 25 mA). 3.5 µl of axoneme were applied to the pretreated grids and blotted by the Vitrobot Mark IV using blot force 3, blot time of 5 seconds, and drain time of 0.5 seconds.

Cryo-EM data acquisition

Movies of the DMTs were acquired at 64kx nominal magnification (calculated pixel size of 1.370 Å/pixel) with counting mode using Titan Krios 300 kV FEG electron microscope (Thermo Fisher Scientific) with the direct electron detector K3 Summit (Gatan, Inc.) and the Bioquantum energy filter (Gatan, Inc.). The data were acquired using SerialEM (*15*). The WT and MEC-17 dataset were collected using a total dose of 45 electrons per $Å^2$ over 40 frames. The K40R dataset was with a total dose of 73 electrons per $Å^2$ per frame over 30 frames. The defocus range was between -1.0 and -3.0 µm.

Cryo-EM image processing

The movies were motion corrected and dose-weighted using MotionCor2 (*16*) implemented in Relion3 (*17*) and the contrast transfer function parameters were estimated using Gctf (*18*). After discarding micrographs with apparent drift and ice contamination, bad contrast transfer function

estimation (3,074, 2410, 4283 micrographs for WT, K40R and MEC17 combined data, respectively). K40R and MEC17 data were merged since the ODA structures were the same in both mutants (Yang, S. et al., manuscript in preparation). The filaments were picked using e2helixboxer (*19*).

The particles of 512 x 512 pixels were initially picked with 8-nm periodicity, binned twice and pre-aligned using a modified version of the Iterative Helical Real Space Reconstruction script (*20*) in SPIDER (*21*) to work with non-helical symmetry. After that, the alignment parameters were transferred to Frealign and the particles were aligned by Frealign for 6 iterations (*22*). The alignment parameters were then converted into Relion 3.0. The particles were scaled to 1.744 Å/pixel (box size 402 pixel) for image processing to reduce memory usage. The 8-nm particles then underwent iterative per-particles-defocus refinement and Bayesian polishing in Relion 3.

The signal of the tubulin lattice was subtracted from each particle. The subtracted particles were subjected to 3D classification into three classes to obtain the 24-nm repeat particles with the ODA in the center. The 24-nm particles were then refined, resulting in resolution of 4.3 and 3.9 Å for WT and K40R from 71,462 and 139,548 particles respectively. At this point, it is clear that the WT doublet did not retain a lot of ODA, only the docking complex (Fig. S1D and E). Therefore, we continued the next step with the K40R and MEC17 combined dataset.

The 24-nm particles were boxed out at a box size of 804 pixel at 1.744 Å/pixel and underwent Bayesian polishing. The ODA are then centered and boxed out of the imaging using the Localized Reconstruction in Scipion (*23, 24*). The particles containing the ODA were then refined using Relion3 and cryoSPARC (*17, 25*). We first refined a single entire ODA region (Fig. S2A). Then, we refined the ODA tail and head regions separately using focus refinement with masks for different regions (Fig. S2B). The resolutions for different regions of the ODA are in the range of 5.5 to 7Å (Fig. S2B and C).

Model building of the ODA complex on the doublet.

First, the Shulin-ODA complex model was separated into two regions: (1) Dyh3 & IC/LC tower region and (2) Dyh4, 5 & DIC3's WD domain. These two regions were rigid body fitted into the active ODA map based on the tail region. Then, each IC and LC was rigid body fitted one by one

to our cryo-EM map. Dyh3 and Dyh4 were segmented into several regions and further fitted to the density. Since the IC and LC regions were fitted quite well to our map at this point, the density corresponding to ICs and LCs were subtracted from the whole tail map and then the HC regions were fitted to the map more precisely. For the head part, the whole head domains were fitted to our cryo-EM map. We noticed that the linker parts of the Shulin-ODA complex were sticking out since our maps are in post-powerstroke conformations. Thus, the linker part was segmented and fitted separately. For Dyh4, the linker region and LC3 were fitted together to our map and then fitted further separately. Compared with the Shulin-ODA complex, there were some parts of ICs which were structured in our map and modeled (Fig. 1C-E). There was a density not observed in the Shulin-ODA complex associated with Dyh4, and LC4 was tentatively assigned to this region (Fig. 1D and E). Finally, the model was integrated, and refined by Coot (*26*) in our map and real-space refined using Phenix (*27*).

Docking Complex Modeling

DC2 (Q233H6) and DC3 (I7M2C6) of *Tetrahymena* were found by BLASTP from the *Chlamydomonas* DC2 (A8JF70) and DC3 (Q7Y0H2). Their initial models were constructed by MODELLER (*28*) from the DC2 and DC3 structure (PDB 6u42). Q233H6 and I7M2C6 are modelled by Coot in the density of the 24-nm average DMT structure (Fig. S3A), in which the docking complex density is much clearer.

DC1 from *Chlamydomonas* (A8IPZ5) did not yield a homolog in *Tetrahymena* using BLAST. Since we could clearly see a density at the place of DC1 in the density map and DC1 from *Chlamydomonas* is not conserved in humans, we reasoned that there is another coiled coil protein in place of DC1. In humans, CCDC151 is known to be important for the docking complex and causes ciliopathy similar to CCDC114 (human DC2 homolog) (*29, 30*). The human CCDC151 localizes to respiratory ciliary axonemes and interacts with CCDC114 (DC2 homolog). The proposed homolog of CCDC151 in *Chlamydomonas* is ODA10. While this protein is important for the ODA assembly in *Chlamydomonas* (*31*), it does not seem to localize in the axoneme like DC1/2 from the MS pattern (*32*).

When we blasted CCDC151, we found Q22T00 as a homolog. To see the MS profile of Q22T00, MS analyses were performed for untreated and salt-treated doublet samples as described in Dai, D, et al., (*33*). The MS profiles of Q22T00 were similar to DC2 and DC3 (Table S1). The coiled

coil prediction of Q22T00 using COILS program (*34*) also coincided with *Chlamydomonas* DC1 (Fig. S3). Therefore, we concluded that despite the weak conservation, Q22T00 is the DC1 in *Tetrahymena*. We constructed the initial model of Q22T00 to the DC1 using MODELLER (*28*). Q22T00 was then modelled by Coot in the density of the 24-nm average DMT structure (Fig. S3A), in which the docking complex density is much clearer. The secondary prediction of Q22T00 fitted well with helical density observed in the density map. For the extended part of DC1/2, two segments from the coiled-coil region of BICDR1 model (105 -161 aa and 202 - 245 aa from PDB: 6F1T) were fitted to our cryo-EM map.

Visualization

The maps and models are visualized using ChimeraX (*35*).

MD simulation

The inactive Shulin-ODA structure had some missing residues. For MD simulation, we modelled loops for missing regions by MODELLER. At the same time, two intermediated parts of Dyh5 (531-636, 3,270-3,382), and both ends of the Dic2 and Dic3 sequences (1-74, 636-667, and 1-17, 511-670, respectively) were removed. Then, we did a coarse-grained MD simulation using this model. In the model, 1 amino acid was treated as 1 bead and each bead located at the Cα position. The force field for observing dynamics used AICG2+ (*36, 37*). In the AICG2+, the reference structure was assumed as the most stable conformation, and their parameters are defined from the reference of all-atom structures. Recently, AICG2+ represented the conformational change of cytoplasmic dynein, and it clarified the allosteric conformational change cascade of dynein's motor domain (*38*). Here, by comparing the inactive Shulin-ODA model with the active ODA structure on the doublet, we identified chains that keep their binding and chains which change their binding schemes. Based on this information, we adjusted the parameters that determine the attraction between the chains. First, since Dyh3, 4, and 5 clearly have a different contact style, we set the attraction force between these chains to be 0.5 times of the default. Next, since the contacts between Dyh3, Dic2, and the LC tower were not significantly changed, we increased the attraction by a factor of 10 in order to treat this chain as a rigid body. Also, since there was no significant difference between Dyh4 and Dic3 contacts, we increased the force of attraction by a factor of 10. Lastly, the attractive force between Shulin and others was decreased by 0.3 times the default in order to observe the Shulin detachment in a reasonable simulation time. After that, we run the simulations on several systems. We performed 10 simulations for all

systems using CafeMol version 2.1 (*39*). If there is not written additional, each MD simulation took 5×10^7 MD steps, and they were conducted by the underdamped Langevin dynamics at 300K temperature. We set the friction coefficient to 0.02 (CafeMol unit) and default values were used for others.

Supplementary Text

Over the docking complex, there is a layer composed of Dyh3 HC, DIC2's WD domain, LC tower and the C-terminal side of DC1/2. Another layer of Dyh4 and DIC3 is further built onto this layer (Fig. 2A and B). The ODA heads were also in contact with the proximal neighboring ODA tail domains (Fig. 1B and Fig. 2D). More specifically, the head of Dyh3 seems to interact with the N-terminal dimerization domain (NDD) of the proximal ODA Dyh4 tail while the Dyh4 head interacts with DIC3 WD40 domain of the proximal ODA (Fig. 2D). These interactions probably stabilize the alignment of the ODA complex.

The Dyh3 showed more change in configuration with ~90° rotation of the head compared with the inactive form whereas Dyh4 HC showed rather a compressing movement of the head side compared with Shulin-ODA structure (Fig. S4B). These conformational changes are mediated by hinge-like motions between the α-helical bundles (Fig. S4C). The center region (bundle 4-8) of Dyh3 showed a milder conformational change compared with other regions of the Dyh3 since the LC tower is associated with this region. In detail, there is a slight change in conformation of both Dyh3 and LC tower (Fig. S4D and E). The conformational change was due to the association of α-helix bundle 8 of the Dyh3 with LC8/8d (Fig. S4D). This interaction was hindered in the Shulin-ODA complex since Shulin is keeping Dyh3's bundle 8 away from LC8/8d.

Even though there was no other structure covering the Shulin binding sites, the regions involved in the interaction with Shulin were dispersed due to the rearrangement of the tail domain as well as the head domains (Fig. S5F). When the Shulin-ODA structure was docked onto the DMT, the Shulin region did not show a steric clash (Fig. 3A4. These observations agree with our model in which the remodeling of the ODA itself likely causes the detachment of the Shulin.

The linker positions of the ODA complex on the DMT are in the post-powerstroke conformation (Fig. S5A). Therefore, the heads are now able to undergo conformational change to the next pre-powerstroke conformation to exert force. With this configuration, LC3 was interacting with Dyh4 AAA+ ring together with the linker. LC3 was interacting with AAA4 of the binding position of the Dyh4 AAA+ ring. However, the binding scheme was different from that of Lis1 which also binds to the AAA3 of cytoplasmic dynein (*40*). LC3 still interacts with AAA4 but it was closer to AAA3 (Fig. S5B). LC1 was previously shown to bind to the MTBD of Dyh3 head (*41, 42*). LC3 is the second component found to be associated with the head domain of the ODA complex. Since LC3

was interacting with AAA+ ring, we carefully examined the linker position of Dyh4. The linker was going at the middle of the apo state and the ADP state and slightly leaning toward AAA4 (Fig. S5C). This is a novel configuration of dynein linker. Previous cryo-ET studies revealed that the β-HC of the sea urchin sperm (equivalent to the Dyh4 of *Tetrahymena*) can undergo an ATPase cycle (*5*). Therefore, in the ATP cycle of the Dyh4, the linker and the LC3 should detach from and re-attach to the AAA+ ring (Fig. S5D). LC3 is a thioredoxin component which was proposed to regulate the ODA activity in response to redox state of the cilia (*43*). Since LC3 was shown to interact with other proteins within the cilia depending on the redox state, LC3 might recruit other regulatory proteins to the Dyh4 AAA+ ring to modulate its motor activity.

Author Contributions

KHB and MI designed the experiments. JG generated mutant *Tetrahymena* strains. SKY and CB performed culture of the cells, purification of microtubule fractions from cilia with the help of DD and MV. SKY and CB performed vitrification of the grids and collected data. SKY, SK and KHB performed the cryo-EM data analysis of the doublet. MI generated a model of the ODA complex on the doublet. SK performed the MD simulation. SK, MI and KHB interpreted the structure. All authors were involved in the manuscript writing process.

Supplementary Figures.

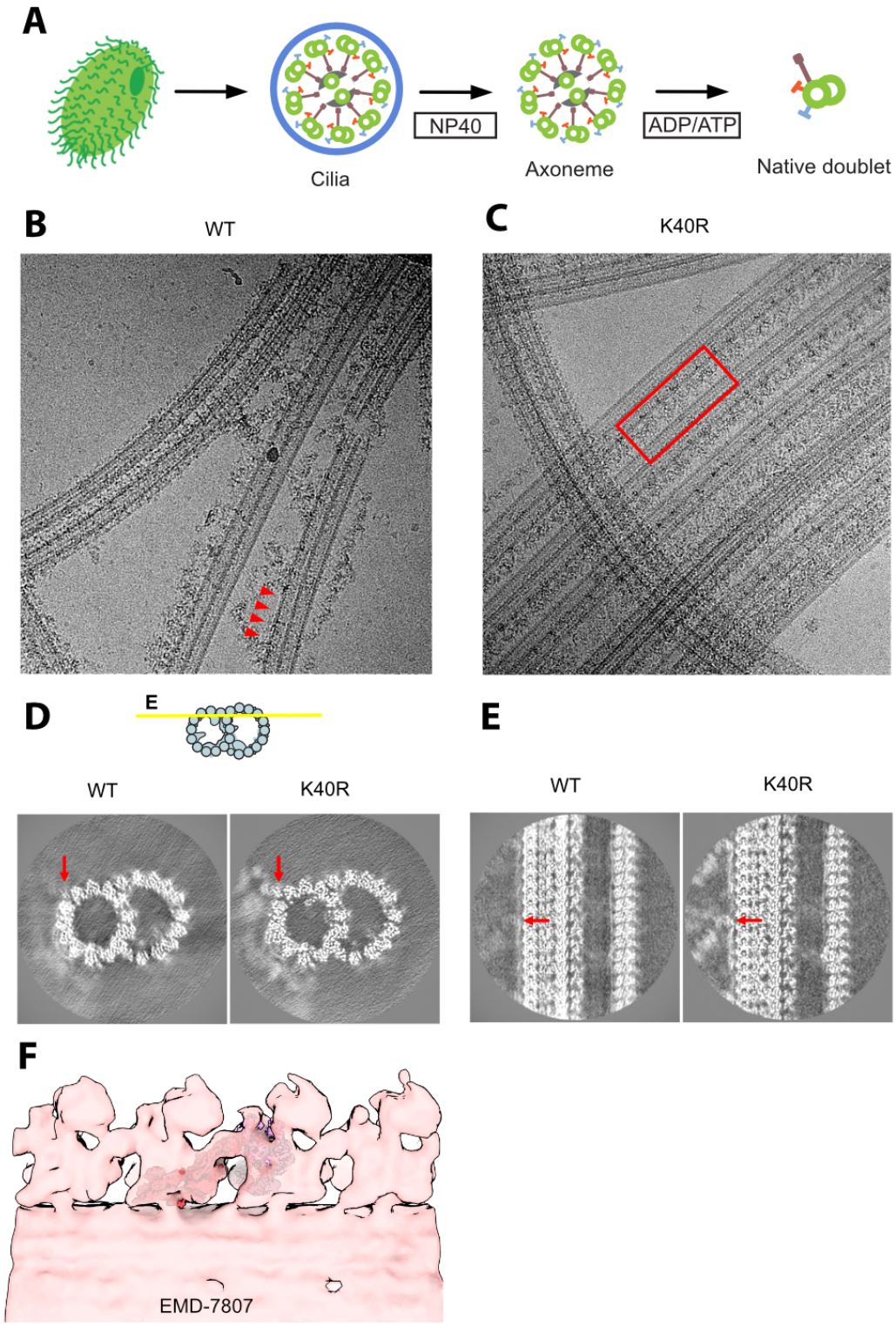

Supplementary Figure 1. Sample preparation and cryo-EM of the DMTs.
(A) The schematic of our isolation strategy for the intact DMTs. In our previous studies of the DMT structures, the ODA complexes were removed by high-salt treatment from doublets (*44-46*). Here, high salt treatment was not performed for the samples. (B, C) Micrographs of DMTs from *Tetrahymena* WT (B) and K40R mutant (C). The red rectangle indicates the row of the intact ODA in the K40R mutant. Red arrowheads indicate region with the detached ODAs. (D, E) 24 nm-structure of doublet from WT and K40R showing the DC is intact in both cases while the ODA is clearly present only in K40R. Red arrows indicate the docking complex. (F) Fitting of our high-resolution structure into the tomographic map of *Tetrahymena* showing it is physiological (ΔRib72B mutant rescued with Rib72B-GFP) (EMD-7807, (*47*)).

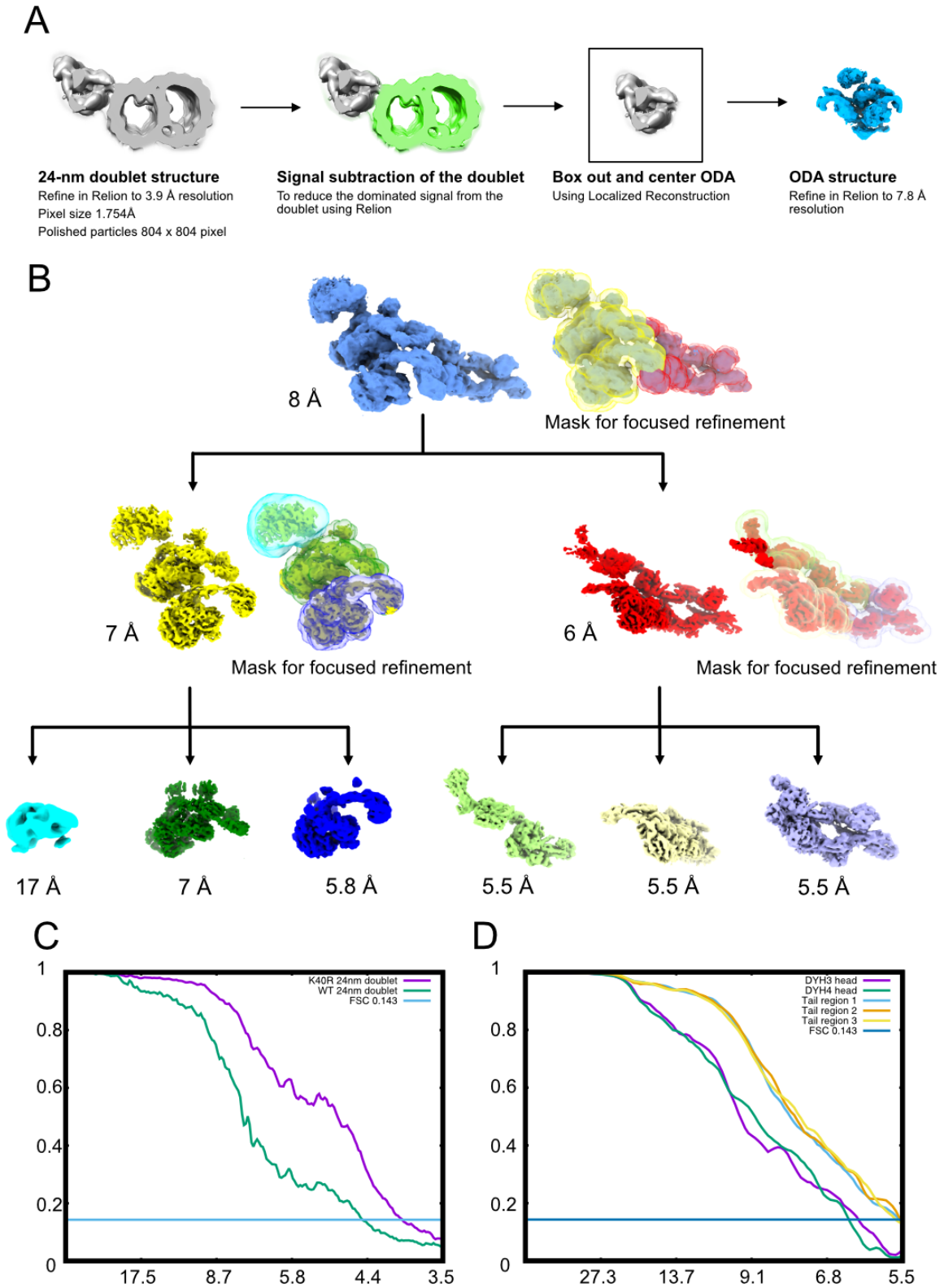

Supplementary Figure 2. Cryo-EM processing strategy

(A) Alignment strategy for the ODA particles. First, we obtained the 24-nm doublet structures. After that, we performed signal subtraction of the DMT. We centered and boxed out the ODA particles and performed refinement of the entire ODA particles. (B) Focus refinement strategy for different regions of the ODA complex. The Dyh5 seems to be too flexible, therefore we can only obtain Dyh5 head at 18-Å resolution. (C) Fourier Shell Correlation of the doublet of WT and K40R & MEC17 combined data. (D) Fourier Shell Correlation of the different regions of the ODA complex by focus refinement.

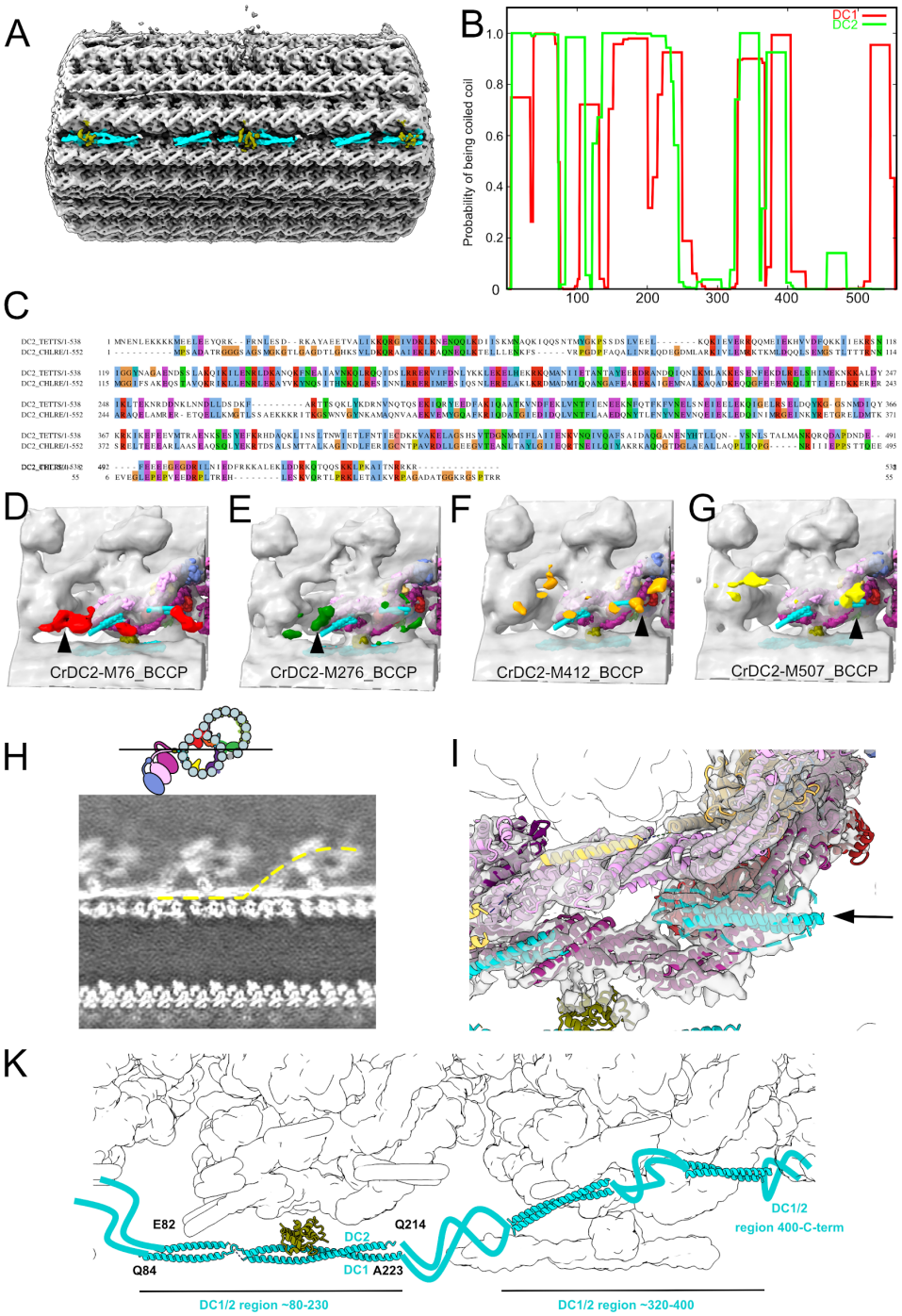

Supplementary Figure 3. Modelling of the Docking Complex.

(A) The DC density on the DMT between PF A7 and A8. (B) Prediction of coiled coil for DC1 and DC2 using COILS with a window size of 28. (C) Sequence alignment of *Chlamydomonas* DC1 and *Tetrahymena* CCDC151 homolog (Q22T00). (D, E, F, G) Structures of *Chlamydomonas* ODA reconstituted on microtubules with Biotin carboxyl carrier protein (BCCP) tagged in different regions of DC2 (residue 76, 276, 412 and 507) from Oda, T. et al., (2016) (*3*) (EMD-6508, 6509,

6510, 6511). The enhanced signals of BCCP-tag are indicated in colors. (H) Slice from a density map showing the connection of the docking complex (position indicated in the cartoon). The yellow line indicates one continuous DC1/2. (I) The globular density at the end of the coiled coil of DC1/2 (black arrow and dotted line). (K) The model of the DC based on our analysis.

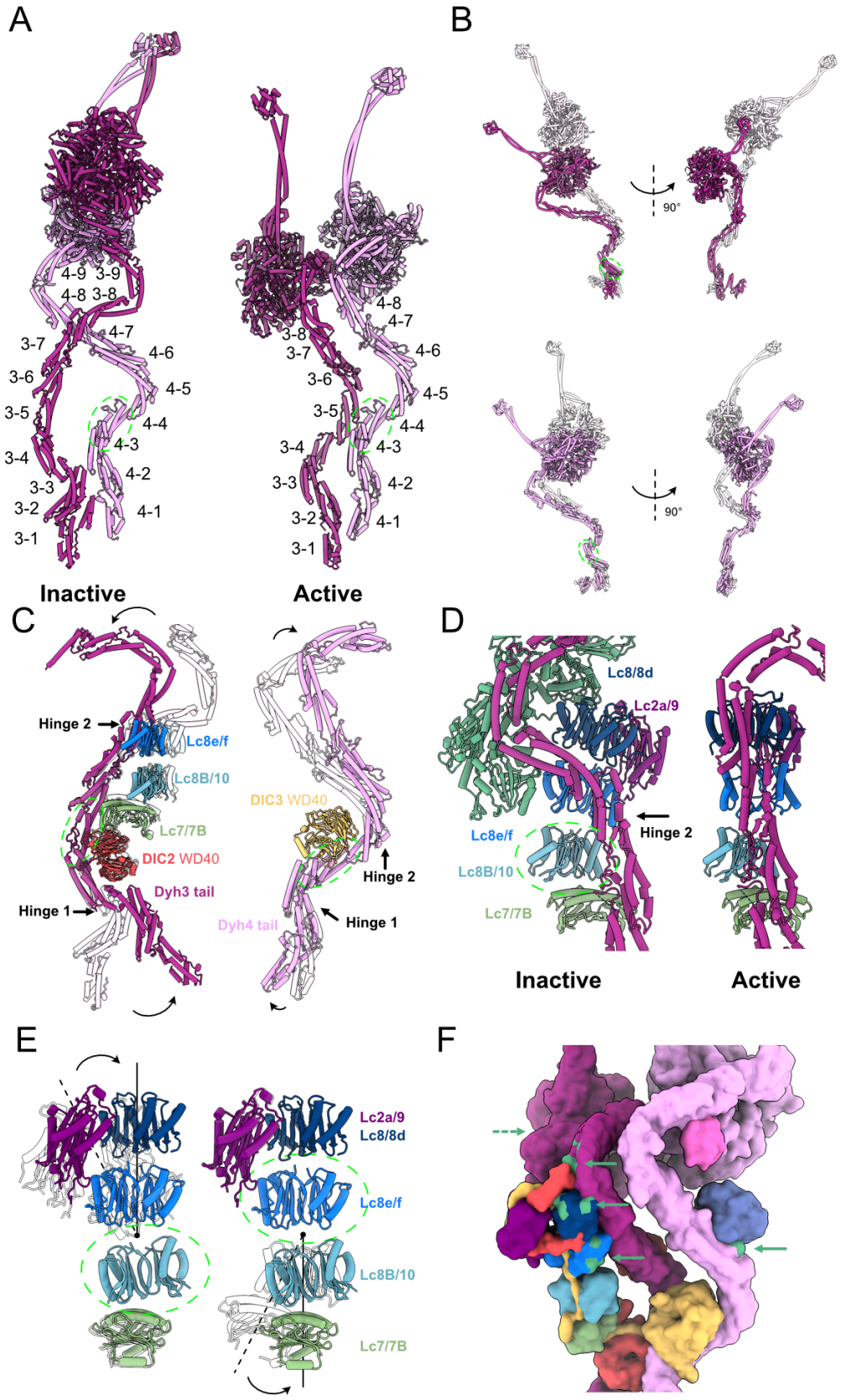
A
4-9
3-9
4-8
3-8
4-7
3-7
4-6
3-6
4-5
3-5
4-4
4-3
3-4
4-2
3-3
3-2
4-1
3-1
Inactive
Active
B
90°
90°
C
Hinge 2
Lc8e/f
Lc8B/10
Lc7/7B
DIC2 WD40
Dyh3 tail
Hinge 1
DIC3 WD40
Hinge 2
Dyh4 tail
Hinge 1
D
Lc8/8d
Lc2a/9
Lc8e/f
Hinge 2
Lc8B/10
Lc7/7B
Inactive
Active
E
Lc2a/9
Lc8/8d
Lc8e/f
Lc8B/10
Lc7/7B
F

Supplementary Figure 4: Data related to the remodeling of the ODA complex.
(A) The labeling of helix bundles in the inactive and active Dyh3 and Dyh4. Inactive and active structures are aligned on helix bundle 4 of Dyh4 (4-4, residues 414-513). (B) Conformational change of the Dyh3 and Dyh4. Alignment of the inactive and active Dyh3 at helix bundle 3 (3-3, residue 448-536) showing ~90° rotation of the head domain (top). Alignment of inactive and active Dyh4 at helix bundle 3 (4-3, residue 414-513) showing compressing conformational changes (bottom). (C) Superimposition of Dyh3 and Dyh4 tails between the inactive (transparent color) and the active ODA. Dyh3 is aligned based on res. 535-646 (helix bundle 5) while Dyh4 is aligned on res. 414-513 (helix bundle 4). The Dyh3 tail exhibits two hinges with larger rotations while the Dyh4 tail also exhibits two hinges with smaller rotations. (D) The changes in interaction between Dyh3 tail and the LC tower due to the remodeling of the inactive to active conformations (two structures are aligned based on Lc8b/10). The conformations of Dyh3 bundle 8, Lc8/8d and Lc2a/9 are significantly different. The release of the Shulin leads to the rotation of the Dyh3 tail, which causes the different interaction pattern between Dyh3 and LC8/8d. (E) Bending conformational change of the LC tower. LC tower from the active ODA complex is in colors and the LC-tower from the Shulin-ODA is shown in transparent. LC towers are aligned based on either Lc8B/10 (left) or Lc8e/f (right) as indicated by green dashed circles. (F) Regions of the ODA that interact with Shulin in the inactive conformation (green regions with green arrowhead) are spread out in the active conformation. The dash arrow indicates the region of Dyh3 head interacting with C3 domain of Shulin, now at the back of the view.

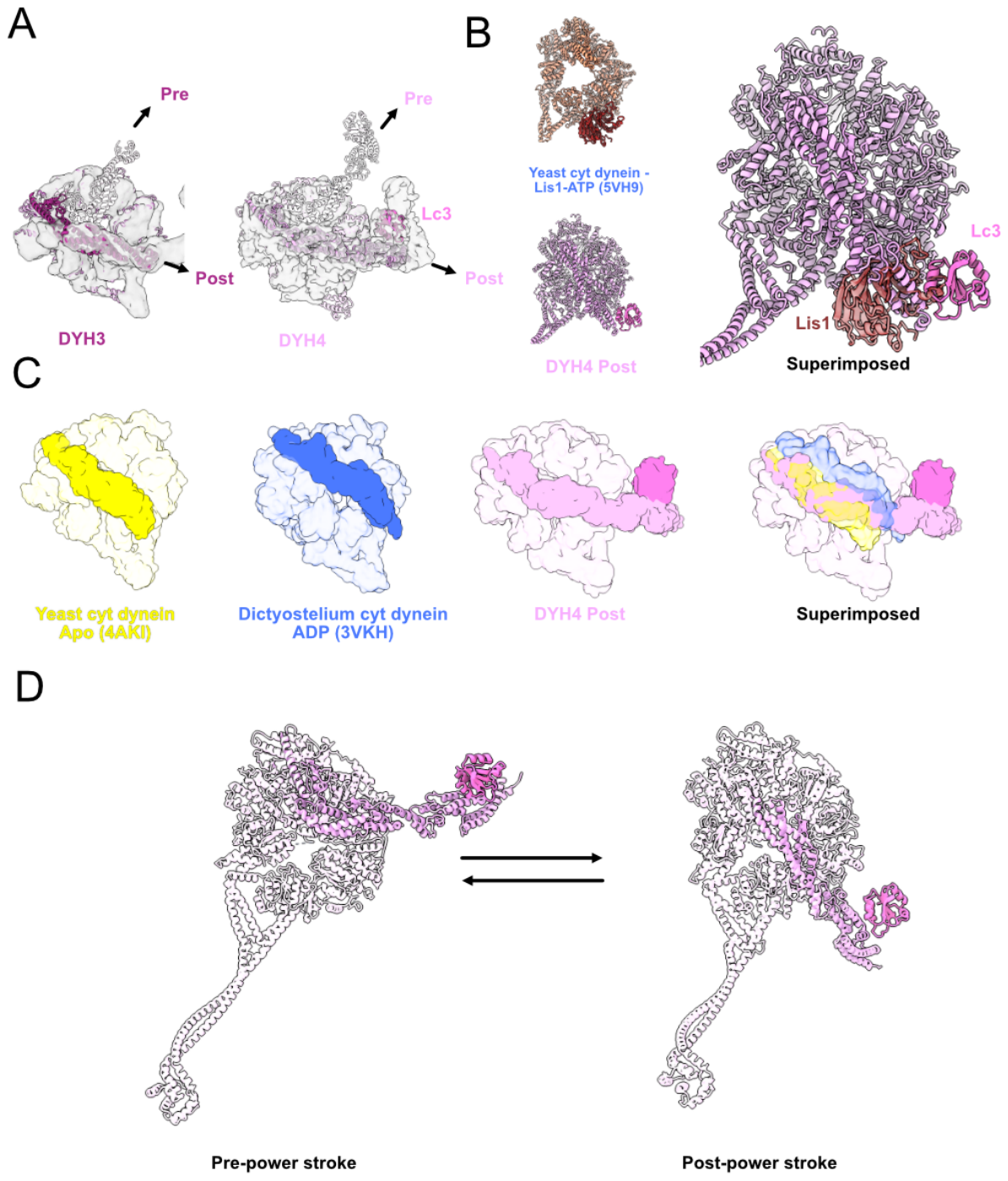

Supplementary Figure 5: Structure of the head domain in ODA on the doublet.
(A) Models of the Dyh3 and Dyh4 heads in post-powerstroke conformations are fitted in the cryo-EM maps of the ODA on the doublet. The Dyh3 and Dyh4 linkers in pre-powerstroke conformations in the inactive Shulin-ODA model are also superimposed (shown in transparent).

(B) Comparison of yeast cytoplasmic dynein bound to Lis1 (PDB: 5VH9) with the Dyh4 bound to LC3. LC3 also binds to the AAA+ ring but in an opposite site from Lis1. (C) Comparison of the linker of Dyh4 in post-powerstroke conformation with the yeast cytoplasmic dynein in apo state and Dictyostelium cytoplasmic dynein in ADP state reveals that the Dyh4 linker is positioned in between of the linker positions in apo and ADP states. The structures are aligned based on the AAA+ ring without linker. (D) Model for the conformation changes from pre-powerstroke to post-powerstroke in Dyh4.

Supplementary Table

Supplementary Table 1: MS total spectrum count of ODA components from *Tetrahymena* WT doublet using native purification of K40R, WT and WT with twice NaCl treatment. In the NaCl treated doublet, most of the ODA components are washed out.

Name	**Name**	**UniprotID**	**K40R**	**WT**	**WT (NaCl)**
Heavy chain	Dyh3	Q22A67	239,232,229	263,250,245	1,0,0
	Dyh4	I7M9J2	259,241,247	264,255,240	0,0,0
	Dyh5	I7M6H4	223,215,199	239,241,218	2,2,0
Intermediate chain	Dic2	I7M008	36,32,31	38,37,32	6,10,9
	Dic3	Q23FU1	40,38,37	38,39,35	15,11,12
Light chain	Lc3	A4VD75	9,9,7	7,7,6	0,0,0
	Lc4a	Q22C78	5,5,3	3,3,2	0,0,0
	Lc1	I7M1N7	22,22,20	19,17,18	0,0,0
	Lc2a	Q1HGH8	4,4,4	5,5,5	1,3,0
	Lc9	A4VEB3	4,3,3	5,5,3	0,0,0
	Lc8	W7XJB1	5,4,4	3,4,3	0,0,0
	Lc8d	Q24CE5	7,6,5	7,7,5	0,0,0
	Lc8e	Q24DI9	3,2,3	1,3,2	0,0,0
	Lc8f	Q22R86	4,4,5	3,4,5	0,0,0
	Lc10	I7MCM8	2,0,2	0,2,0	0,0,0
	Lc8b	A4VE64	6,6,6	2,2,0	0,0,0

	Lc7	I7MHB1	8,8,8	6,7,7	0,3,3
	Lc7b	Q1HFX1	6,4,5	5,5,4	0,0,0
	Lc7a*	Q1HFX2	4,4,4	3,3,3	0,0,0
	Lc2b*	I7M0N9	4,6,6	4,4,4	0,0,0
	Tct1a*	I7MGG2	0,0,0	0,0,0	0,0,0
	Tct1b*	Q231T5	2,2,2	0,0,0	0,0,0
Docking Complex	DC1	Q22T00	29,26,28	27,26,22	0,0,2
	DC2	Q233H6	20,19,17	24,25,24	0,3,2
	DC3	I7M2C6	15,13,11	17,16,17	4,3,4

* Components not present in ODA according to (*10*)